論文 / 著書情報
Article / Book Information

Title	Role of bonding structure in the corrosion resistance and tribological properties of Tantalum-containing carbon coating: An analysis employing various deposition bias voltages
Authors	Lulu Li, Takayuki Tokoroyama, Ruixi Zhang, Wenjun Wu, Xue Fan, Nan Jian, Dongfeng Diao, Noritsugu Umehara
Citation	Tribology International, Vol. 213, No. 111014, pp. 1-13
Pub. date	2026, 1
DOI	https://dx.doi.org/10.1016/j.triboint.2025.111014
Creative Commons	Information is in the article.

Tribology International 213 (2026) 111014

Contents lists available at ScienceDirect

Tribology International

journal homepage: www.elsevier.com/locate/triboint

Full length article

Role of bonding structure in the corrosion resistance and tribological properties of Tantalum-containing carbon coating: An analysis employing various deposition bias voltages

Lulu Li [a], Takayuki Tokoroyama [a,*], Ruixi Zhang [a,b], Wenjun Wu [a], Xue Fan [c], Nan Jian [c], Dongfeng Diao [c], Noritsugu Umehara [a]

[a] *Department of Micro-Nano Mechanical Science and Engineering, Graduate School of Engineering, Nagoya University, 464-8603, Japan*
[b] *Laboratory for Future Interdisciplinary Research of Science and Technology (FIRST), Institute of Integrated Research (IIR), Institute of Science Tokyo, 226-8501, Japan*
[c] *Institute of Nanosurface Science and Engineering (INSE), Guangdong Provincial Key Laboratory of Micro/Nano Optomechatronics Engineering, Shenzhen University, 518060, China*

ARTICLE INFO

Keywords:
Coating
TaC
TEM
Corrosion
Wear

ABSTRACT

The research clarified the relationship between applied deposition bias voltage and the resulting bonding structure evolution, which directly adjusts corrosion resistance and tribological properties of multilayered tantalum-containing carbon coatings. Comparative analysis of bonding structure revealed that the preferential orientation of the tantalum carbide structure shifts from TaC (200) to TaC (111) as the bias voltage ranges from −75 V to −125 V. The TaC (111) structure significantly enhances chemical stability and anti-deformation ability, contributing to low corrosion current and specific wear rate. The graphite structure formed in the coating deposited at a bias voltage of −175 V effectively contributed to the lowest friction coefficient. However, the friction advantage is accompanied by decreased mechanical strength and accelerated wear.

1. Introduction

With the automotive industry toward electrification, Japanese manufacturers are increasingly concerned with tribological challenges in ester-based lubricant systems used in modern powertrains. Ester-based lubricants exhibit heightened corrosivity compared to traditional mineral-based lubricants. The chemical interactions between corrosive environments and metal surfaces often generate localized degradation, including pitting and delamination, compromising structural integrity and creating a synergistic acceleration of wear [1]. Addressing these challenges requires advanced surface engineering solutions capable of simultaneously providing barrier protection against chemical corrosion, maintaining low-friction interfaces, and excellent mechanical strength in aggressive chemical environments. Among the various protective technologies, Diamond-Like Carbon (DLC) coatings have emerged as valuable surface engineering solutions due to their exceptional mechanical durability and self-lubricating characteristics [2–10]. Although several studies have documented the corrosion resistance of certain DLC coatings, systematic research exploring the optimization of the coatings specifically for aggressive chemical environments remains underdeveloped. Combining mechanical strength, tribological properties, and chemical stability is increasingly critical for advanced engineering applications [11–14].

The mechanical performance of carbon coatings is fundamentally related to their bonding structure. The tetrahedral amorphous carbon (ta-C) structures characterized by predominant sp^3 hybridization exhibit superior hardness values [15–22]. This property advantage can be maintained even with the incorporation of metallic dopants. Previous investigations by our research group have focused on tantalum-containing coatings [10,23,24], where we observed that controlled tantalum incorporation could be achieved without compromising the hardness of the ta-C structure while simultaneously reducing the friction coefficient. A notable advantage of tantalum-containing coatings is their dual functionality: they stabilize the carbon network against oxidative degradation while simultaneously forming passive tantalum oxide that improves the chemical stability of the coatings in corrosive environments. Therefore, further investigation into corrosion resistance, friction behavior, and wear properties of tantalum-containing ta-C coatings (ta-C: Ta) in corrosive environments is warranted. Layer structure design is crucial in controlling the bonding

---

* Corresponding author.
E-mail address: takayuki.tokoroyama@mae.nagoya-u.ac.jp (T. Tokoroyama).

https://doi.org/10.1016/j.triboint.2025.111014
Received 6 May 2025; Received in revised form 10 July 2025; Accepted 20 July 2025

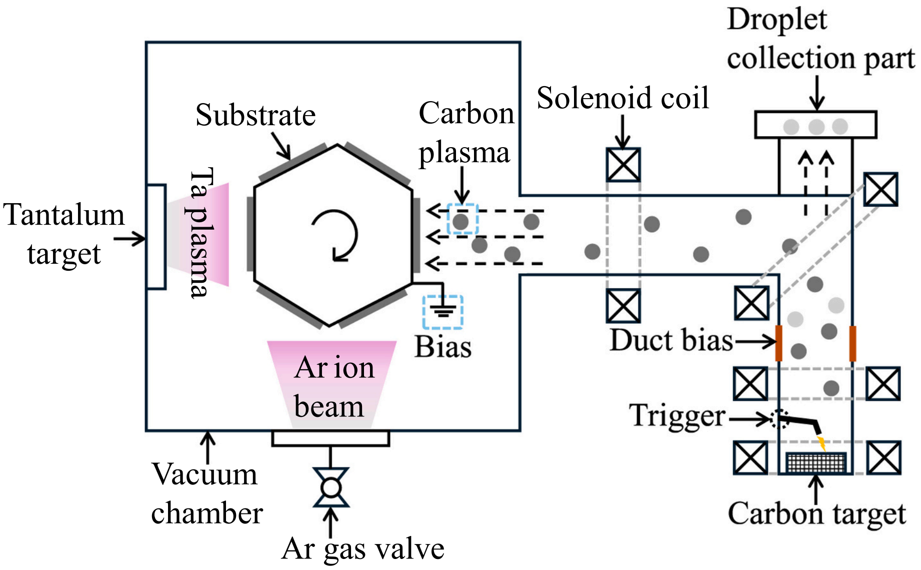

Fig. 1. The schematic of the IBA-FAD deposition system.

structure and minimizing defects. Our earlier research designed a bilayer structure comprising a ta-C bottom layer followed by a Ta-containing top layer, with a combined thickness of 300 nm, that delivered exceptional resistance to corrosive wear. This enhanced performance was attributed primarily to the emergence of protective tantalum-based oxide along the wear interface [25]. Based on the bilayer structural design, deposition parameters are also crucial in controlling the cross-sectional bonding structure and defect characteristics [26–30]. Fayed et al. [26] reported that the deposition bias voltage is a main factor in increasing the coating density and decreasing the surface roughness with the deposition bias voltage increasing from 100 V to 300 V, corresponding to the enhanced corrosion resistance. Ren et al. [27] designed various hydrogen-free DLC coatings deposited at bias voltage from 0 to −100 V, which exhibited corrosion current of 4.53 $\mu A/cm^2$ when the deposition bias voltage of −75 V. They found that deposition bias voltage influences the energy and rate of the plasma depositing on the substrate, which in turn affects the defect characteristics, bonding structure, and corrosion resistance of the coating. Han et al. [28] developed DLC coatings using deposition bias voltages ranging from 0 to −200 V (with various bias gradient rates) over 60 min. The DLC coating deposited with a −25 V gradient demonstrated superior wear resistance due to the hardness and elevated C-C sp^3 bond content. The results demonstrate that deposition bias voltage is an important parameter affecting coating properties and application in corrosive environments.

This paper investigates the application of bilayer coatings (ta-C bottom layer followed by a ta-C: Ta top layer) in corrosive environments, focusing on how the applied bias voltage affects corrosion resistance, friction behavior, and wear properties. Given the difficulty of replicating proprietary corrosive environments across industries, we employed the 3.5 wt percent sodium chloride solution as a representative corrosion and tribology test medium. Our analysis examines three critical aspects: (1) the relationship between carbon-tantalum bonding structures and corrosion resistance, (2) the correlation between wear surface properties and resulting friction behavior, and (3) the role of microstructural features (specifically tantalum carbide nanocrystals and graphite structure) in determining mechanical strength and wear resistance.

Table 1
Deposition parameters for coatings prepared at various bias voltages.

Coating structure	C target current, A	Ta target current, A	Ar flow, ml/min	Deposition Bias voltage, V
ta-C	60	0	2	−75, −100, −125, −150, −175
ta-C: Ta	80	0.3	12	

2. Experimental procedure

2.1. Coating deposition procedure

A cylindrical tungsten carbide (WC) disk with a diameter of 22.4 mm was selected as the substrate material for coating deposition. Prior to being placed into the vacuum system, the WC surfaces underwent sequential solvent cleaning utilizing benzene, followed by acetone to ensure the removal of contaminants. Coating was prepared using an Ion Beam Assisted-Filtered Arc Deposition (IBA-FAD) system [31], with the equipment illustrated schematically in Fig. 1. The pre-deposition process comprised two primary steps: initial chamber evacuation to establish a base pressure of 4.0×10^{-3} Pa, controlled introduction of argon gas (flow rate: 18 ml/min) for generating energetic ions accelerated at 1.8 kV. These ions bombarded the substrate surface for 20 min, facilitating both contaminant removal and surface activation to promote adhesion with the subsequently deposited coatings. The coating deposition process comprised two primary steps: (1) Tantalum plasma was synthesized with energetic Ar^+ (argon gas flow rate: 15 ml/min) bombarding the Ta target (target current of 0.3 A), forming a pure tantalum interlayer. (2) The coating structure was developed through an undoped ta-C bottom layer followed by a ta-C: Ta top layer. During the deposition process, carbon plasma was generated from the ignited carbon target and deposited at a 90-degree angle to the WC substrate. We prepared coatings at bias voltages of −75 V, −100 V, −125 V, −150 V, and −175 V, controlling the deposition time to maintain a consistent coating thickness of about 365 nm. Table 1 lists the specific deposition parameters.

2.2. Corrosion test procedure

Electrochemical measurements were conducted using a HAL3001A system (manufactured by Meiden Hokuto Denko, Japan) incorporating

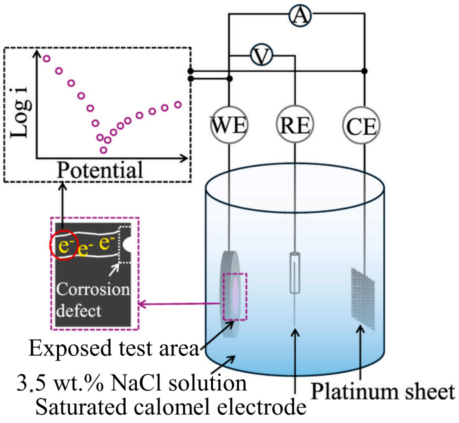

Fig. 2. The schematic of the three-electrode measurement system.

an HB-305 potentiostat/galvanostat unit. We employed a conventional three-electrode system as illustrated in Fig. 2. This system featured a saturated calomel reference electrode (RE) establishing the potential measurement circuit, a platinum counter electrode (CE) for current circulation, and the coating specimen serving as the working electrode (WE). The coating specimen was positioned in the testing cell, and a consistent electrolyte-exposed surface area of 0.8 cm^2. The test environment consisted of 3.5 wt percent sodium chloride solution at room temperature. Prior to conducting potentiodynamic polarization (PDP) measurements, each coating specimen underwent a 30-minute equilibration period until achieving a stable state. Subsequently, polarization scans were initiated from a cathodic potential of -0.7 V and toward anodic potential up to $+ 0.7$ V, with potential controlled at a constant rate of 1 mV per second. Analysis of the resulting polarization curves employed the standard Tafel extrapolation technique [32,33]. Additionally, polarization resistance (Rp) was determined through the following Stern-Geary relationship:

$$R_p = \frac{\beta_a \times \beta_c}{2.303 i_{corr}(\beta_a + \beta_c)}$$

where $\beta_a$and β_c correspond to the Tafel gradients in anodic and cathode directions.

2.3. Tribological testing procedure

Tribological evaluations were performed on a designed ball-on-disk tester. The system incorporated force sensors that continuously measured frictional force and converted it to the friction coefficient. The tribological interface consisted of a tungsten carbide (WC) sphere (radius of 4 mm) mounted in a specialized holder. Testing was performed with the coating specimen (coated disk) fully submerged in the 3.5 wt percent sodium chloride solution. During the test, coating specimens underwent rotational contact at a vertical loading force of 10 N applied to the stationary WC sphere. The coating specimen was subjected to continuous rotation at a fixed angular velocity of 150 revolutions per minute, with the contact position at a 4 mm radial distance from the center of rotation. To increase the reliability of the results, each coating specimen was tested three times. For quantitative wear analysis, non-contact optical profilometry was employed to characterize the wear scar geometry and calculate the specific wear rate by integrating cross-sectional profiles from multiple positions along the wear scar.

2.4. Coating characterization

The chemical bonding structures at both the coating surface and through the coating thickness were characterized using a PHI Quantera X-ray Photoelectron Spectroscopy (XPS) system. Spectral acquisition consisted of twenty sequential measurement cycles to ensure data reliability, with spectral deconvolution performed using MultiPak analytical software. Field emission scanning electron microscopy (FE-SEM, SU-8200, Hitachi) with Energy Dispersive X-ray Spectroscopy (EDS) analysis was used to evaluate as-deposited coating surface morphology. Renishaw in-via Raman system employing 532 nm laser excitation

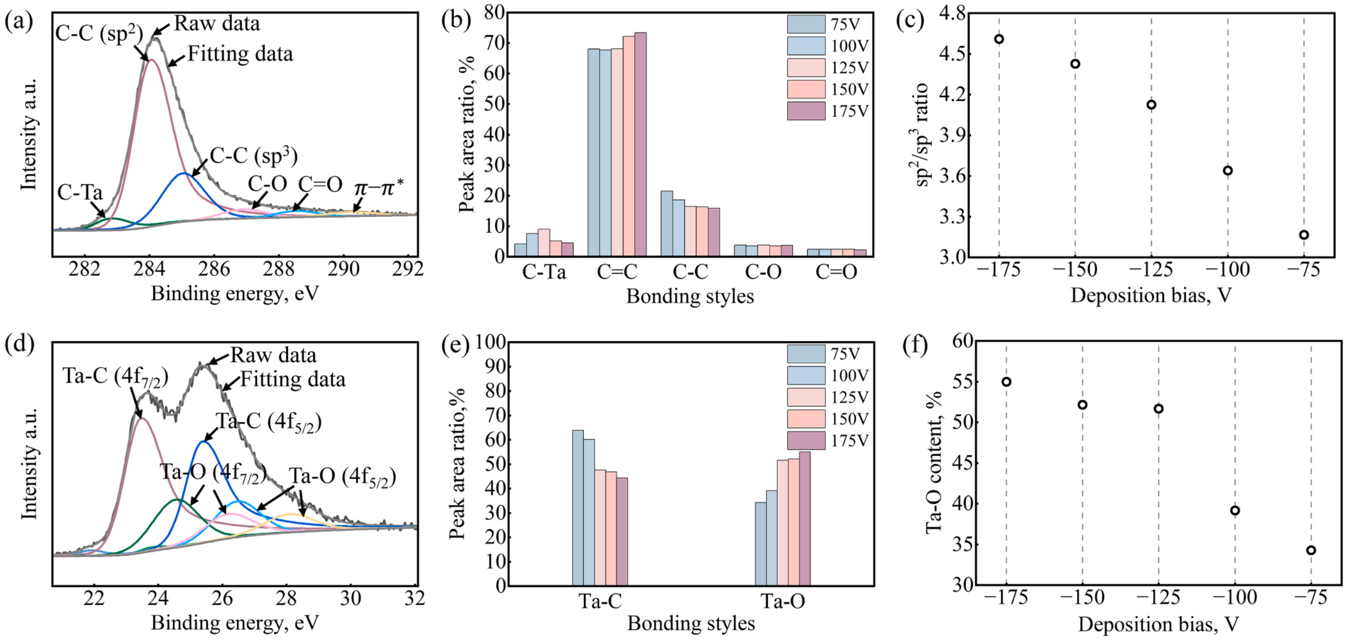

Fig. 3. XPS analysis of coatings (a) C1s deconvolution results of coating at bias voltage of -75 V, (b) deconvoluted C1s peak area ratios of the coatings at bias voltage decreasing from -75 V to -175 V, (c) sp^2/sp^3 ratio of the coatings at bias voltage decreasing from -75 V to -175 V, (d) the Ta4f deconvolution results of coating at bias voltage of -75 V, (e) deconvoluted Ta4f peak area ratios of the coatings at bias voltage decreasing from -75 V to -175 V, (f) Ta-O content of the coatings at bias voltage decreasing from -75 V to -175 V.

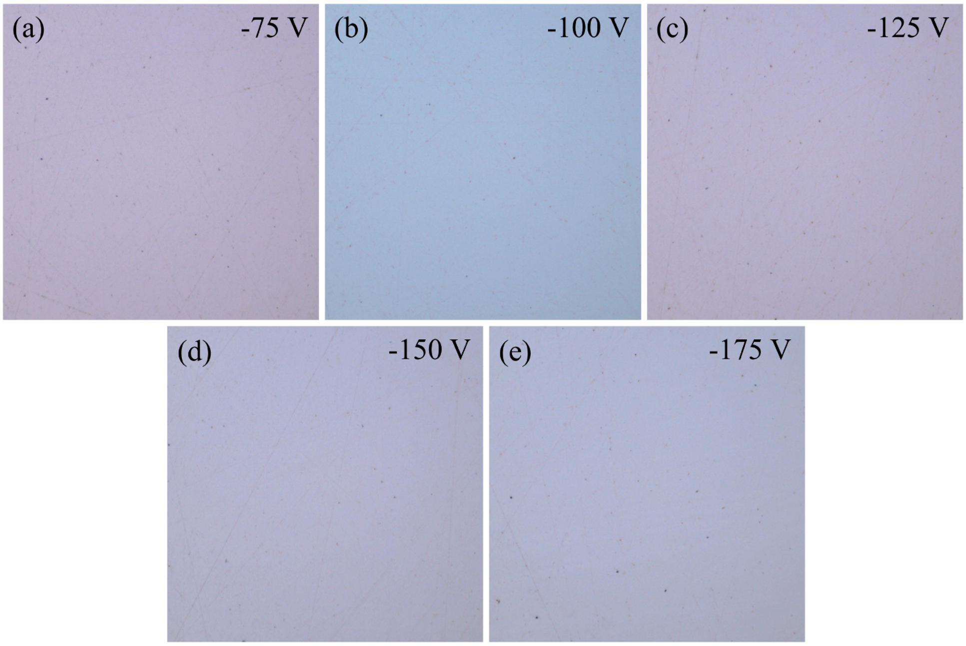

Fig. 4. Surface morphologies of coatings deposited at bias voltages of (a) −75 V, (b) −100 V, (c) −125 V, (d) −150 V, and (e) −175 V.

allowed assessment of carbon hybridization states in as-deposited coatings and the post-test wear surface on the WC sphere. To enable nanoscale structural analysis, cross-sectional view ultrathin coating specimens were prepared using a focused ion beam (FIB, Scios, Thermo Fisher Scientific, USA). During preparation, a protective platinum layer was deposited to preserve coating integrity. Coating structures were subsequently analyzed in a Transmission Electron Microscope (TEM) (FEI-Titan3 Cubed Themis G2 300) featuring double aberration correction, enabling atomic-resolution imaging of crystalline distributions and interfacial structures throughout the bilayers. Hardness measurement for mechanical properties characterization was performed using an Elionix indentation (ENT-5) tester in constant load control mode with a maximum force of 1000 μN. The coating roughness and the characteristics of the as deposited, corroded and worn surfaces were observed using a laser optical microscope. The Image J analytical software employed statistical evaluation of corrosion defect densities across the coating specimen following exposure to the corrosive environment.

3. Results and discussions

3.1. *Structural and morphological characterization of the coatings*

An XPS test was performed to analyze surface chemical bonding structures of coatings. Fig. 3 shows the C1s and Ta4f deconvolution results, deconvoluted peak area ratios, sp^2/sp^3 ratio of carbon structure, and oxidized-bonded Ta-O content. The C1s deconvolution result, illustrated in Fig. 3(a), reveals electronic states corresponding to multiple bonding structures in the carbon network. Binding energies at 282.8 eV, 284.1 eV, 285.1 eV, 286.9 eV, 288.5 eV, and 290.2 eV indicate chemical bonds of C-Ta, C-C sp^2, C-C sp^3, C-O, C═O, and π electron shake-up, respectively [34,35]. The deconvoluted peak area ratios of the above bonds and the typical C-C sp^2/sp^3 ratio results are shown in Fig. 3 (b) and 3 (c). A clear correlation exists between deposition bias voltages and carbon hybridization states. As the bias voltages decreased from −75 V to −175 V, it was observed that a progressive enhancement of the C-C sp^2 bond ratio and the expense of the C-C sp^3 bond ratio, reaching the highest sp^2/sp^3 ratio at a bias voltage of −175 V. The Ta4f deconvolution result is shown in Fig. 3(d), where the binding energies at 23.5 eV (4 $f_{7/2}$) and 25.4 eV (4 $f_{5/2}$) are attributed to tantalum atoms engaged in carbide bonding structure and forming the Ta-C bond. The binding energies at 24.6 eV and 26.5 eV provide evidence of the Ta-O bond formed in the sub-oxidized Ta structures. The higher binding energies at 26.3 eV and 28.2 eV correspond to tantalum atoms in the fully oxidized pentoxide state (Ta_2O_5) [36,37]. The deconvoluted peak area ratios of the above bonds and the total oxidized-bonded Ta-O content results are shown in Fig. 3(e) and 3 (f). Regarding the decreasing deposition bias voltage from −75 to −175 V, it is noteworthy that the Ta-O content increases and reaches the maximum value at the bias voltage of −175 V. The above results indicate that decreasing the deposition bias voltage promotes both graphitization of the coating and the oxidation ability of tantalum atoms on the coating surface.

The as-deposited coating surface morphologies were examined using

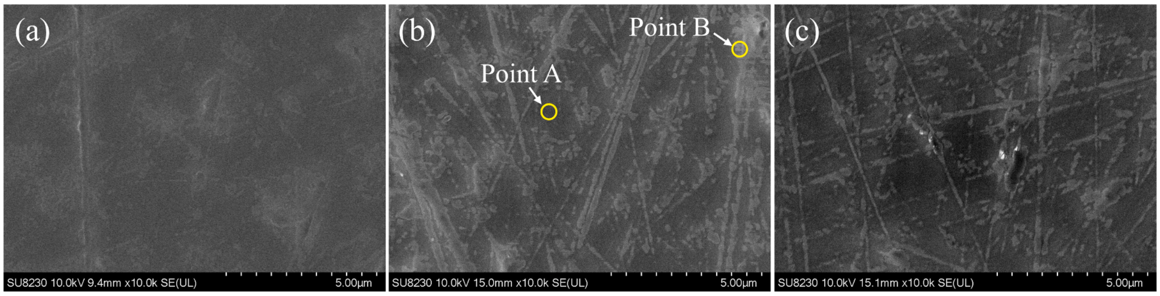

Fig. 5. Surface morphologies observed using a FESEM of the coatings at various bias voltages (a) −75 V, (b) −125 V, (c) −175 V.

Table 2
EDS analysis at selected positions A and B on the coating surface.

Atom percent	C	O	Ta	W
Point A	80.08	1.62	16.60	1.69
Point B	82.04	1.80	14.41	1.74

a laser microscope and FESEM images. Laser microscope images of the coatings (shown in Fig. 4) show that no significant differences were observed among the coating surfaces at various deposition bias voltages, and no obvious pores, cracks, or other defects were detected on the surfaces.

Fig. 5 displays the FESEM surface observation of the coatings. There are no apparent pores, cracks, or other defects on the coating surfaces. To investigate the light-colored striped regions observed on the coating surface, we performed comparative EDS analysis on both the dark and light-colored striped regions on the coating surface (designated as points A and B, respectively). As shown in Table 2, no differences in elemental atomic percentages were found between these two positions. Therefore, we believe that this surface morphology of the coating may be related to micro-grooves that inherently existed during substrate surface machining.

3.2. Corrosion resistance of the coatings

3.2.1. Corrosion test parameters and corroded surface morphology

Electrochemical behavior was evaluated through potentiodynamic polarization (PDP) measurements, comparing the corrosion resistance of the coatings as a function of deposition bias voltage. Fig. 6 displays the polarization curves, fitted corrosion current density (Log i), and

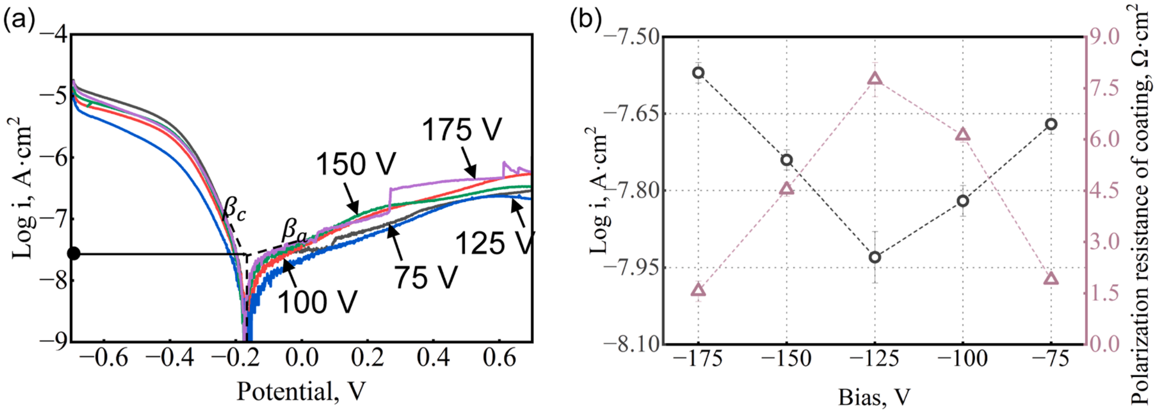

Fig. 6. (a) Polarization curves of the coatings at bias voltage decreasing from −75 V to −175 V, (b) fitted corrosion current density and polarization resistance of the coatings at bias voltage decreasing from −75 V to −175 V.

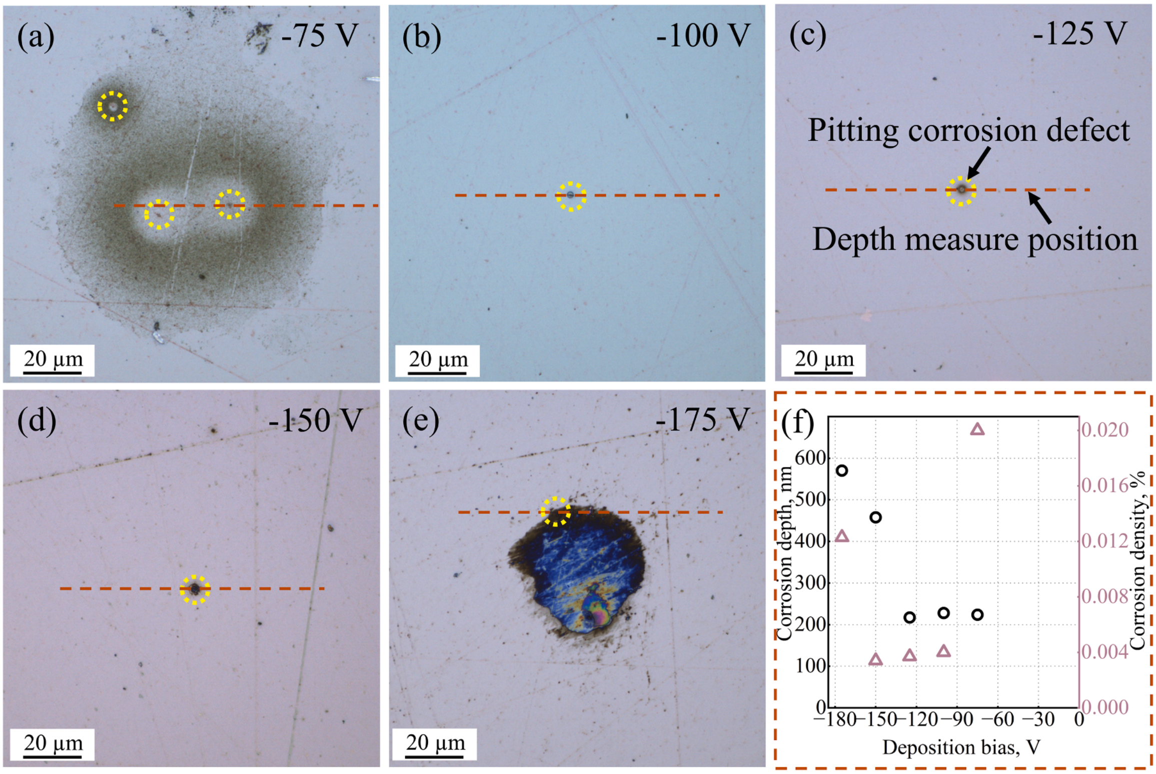

Fig. 7. Corroded surface morphology of coatings deposited at bias voltages of (a) −75 V, (b) −100 V, (c) −125 V, (d) −150 V, (e) −175 V, and (f) corrosion parameters including density and depth.

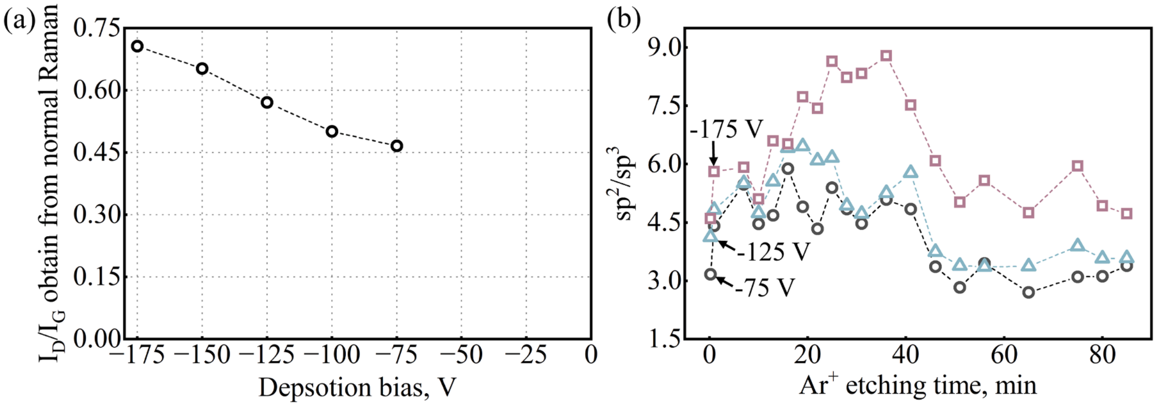

Fig. 8. (a) I_D/I_G ratio of coatings at bias voltage decreasing from −75 V to −175 V (obtained from the Raman spectrum deconvolution), (b) specific sp^2/sp^3 value of the coatings obtained from XPS analysis through coating thickness.

calculated polarization resistance (Rp) of the coatings. Generally, the corrosion current density (Log i) and polarization resistance (Rp) can distinguish the corrosion resistance of the coatings. A higher corrosion-resistant coating typically exhibits lower Log i and higher Rp values [38, 39]. The Log i value initially decreased from −7.67 to −7.93 as bias voltage decreased from −75 V to −125 V, and the Log i value subsequently increased to −7.57 as bias voltage further decreased to −175 V. The Rp value inversely correlates with the Log i value. Consequently, the corrosion resistance of the coatings decreases in the order of −125 V, −100 V, −150 V, −75 V, and −175 V, with the coating deposited at −125 V bias voltage exhibiting the highest corrosion resistance. Fig. 7 shows the morphology of the corroded coating, providing insight into how deposition bias voltage affects the corrosion currents and polarization resistance of the coatings. Observation of corroded coating surface (shown in Fig. 7(a-e)) revealed pitting corrosion defects across all coatings, though with variations in density and depth (shown in Fig. 7 (f)). The pitting corrosion depth remained similar as the deposition bias voltage decreased from −75 V to −125 V, but then increased gradually as the bias voltage decreased to −150 V and −175 V. The coating deposited at a bias voltage of −175 V exhibited the highest corrosion depth. Comparing the corrosion density among the coatings, the coating deposited at a bias voltage of −75 V exhibited the highest pitting corrosion density. The coating deposited at a bias voltage of −125 V showed significantly lower corrosion density compared to that deposited at −75 V. Analyzing the above results, the highest corrosion density of −75 V bias voltage and the highest corrosion depth of −175 V bias voltage may be the factor in the higher corrosion current than that of −125 V bias voltage.

3.2.2. *Corrosion mechanism of the coatings*

Regarding the corrosion resistance of carbon coatings, the surface properties function as crucial determinants of the electrochemical behavior [40]. The increased roughness provides more active sites for initiating corrosion reactions [41]. However, the average surface roughness value is 11.5, 11.4, 11.4, 11.6, and 12.1 nm of the coatings at deposition bias voltage from −75 V to −175 V. A similar roughness value may not be a factor in the various corrosion currents. Regarding the surface properties, the generation of oxide-based protection at the coating surface inhibits the penetration of corrosive species and hinders corrosion reactions [42–44]. Analyzing the deconvoluted Ta-O peak result in Fig. 3(f), it is noteworthy that the Ta-O content reaches the maximum value at the bias voltage of −175 V. However, the coating at the bias voltage of −175 V displays the highest corrosion current. Therefore, the surface properties of the coatings may not be a significant factor in corrosion resistance, and greater focus should be placed on the total cross-sectional structure of the coatings. The cross-sectional carbon structure was characterized using Raman spectroscopy and XPS analysis through the coating thickness. The obtained D peak to G peak height ratio (I_D/I_G) from the Raman spectrum deconvolution and specific sp^2/sp^3 value at various Ar$^+$ etching times are shown in Fig. 8. Analysis of the results in Fig. 8(a) and 8 (b) reveals a monotonic negative correlation between the I_D/I_G ratio and deposition bias voltage. The sp^2/sp^3 values at the same etching times all show a monotonic increase with deposition bias voltage from −75 V to −175 V. However, the monotonic increase of I_D/I_G ratio and sp^2/sp^3 value corresponds to the decrease in chemical stability, which is inconsistent with the tendency of coating corrosion current [45–47].

To clarify the mechanism of how deposition bias voltage affects the corrosion current density and corrosion parameters (including corrosion depth and corrosion density) of the coatings, cross-sectional structures were analyzed using high-resolution transmission electron microscopy (HRTEM) images, with results shown in Fig. 9. No obvious holes or crack defects are visible in the whole cross-section of the coatings (Fig. 9(a-d)), indicating the stability of coating deposition and the uniformity of coating structure. Higher magnification of the boxed regions in Fig. 9(a-d) is shown in Fig. 9(a, b, c, d-1; a, b, c, d-2), which reveals that coatings consist of nanocrystalline structures embedded in an amorphous matrix. Analysis of the nanocrystalline structures (including variations in lattice spacing and diffraction spots characteristics) reveals significant differences in the top ta-C: Ta and bottom ta-C layers deposited at various bias voltages. In the top ta-C: Ta layer, the lattice spacing of 0.221 nm, 0.255 nm, and 0.359 nm corresponds to TaC (200), TaC (111), and graphite structure, respectively. In the bottom ta-C layer, graphite nanocrystals with a lattice spacing of 0.331–0.378 nm are embedded in the amorphous carbon matrix. The coating deposited at a bias voltage of −75 V mainly features TaC (200) nanocrystals embedded in the amorphous carbon matrix. For the coating deposited at a bias voltage of −100 V, both TaC (200) and TaC (111) nanocrystals are embedded in the amorphous carbon matrix. The coating deposited at a bias voltage of −125 V mainly features TaC (111) nanocrystals embedded in the amorphous carbon matrix. With the deposition bias voltage decreased to −175 V, in addition to the TaC nanocrystals formed in the ta-C: Ta layer, distinct graphite structures are also embedded in the amorphous carbon matrix. Additionally, the graphite nanocrystal spacing in the ta-C layer exceeds that in other coatings. The varying nanocrystalline structures in coatings deposited at various bias voltages play a critical role in corrosion resistance. As the deposition bias voltage decreases from −75 V to −125 V, it is noteworthy that the tantalum carbide preferential orientation shifts from TaC (200) to TaC (111), and a denser amorphous carbon structure forms. Compared to the TaC (200) structure, the TaC (111) structure features maximized coordination numbers with stronger bonding strength and higher surface cleavage energy, creating more effective barriers against charge transfer processes, which are essential for reducing corrosion reaction rate and increasing chemical stability

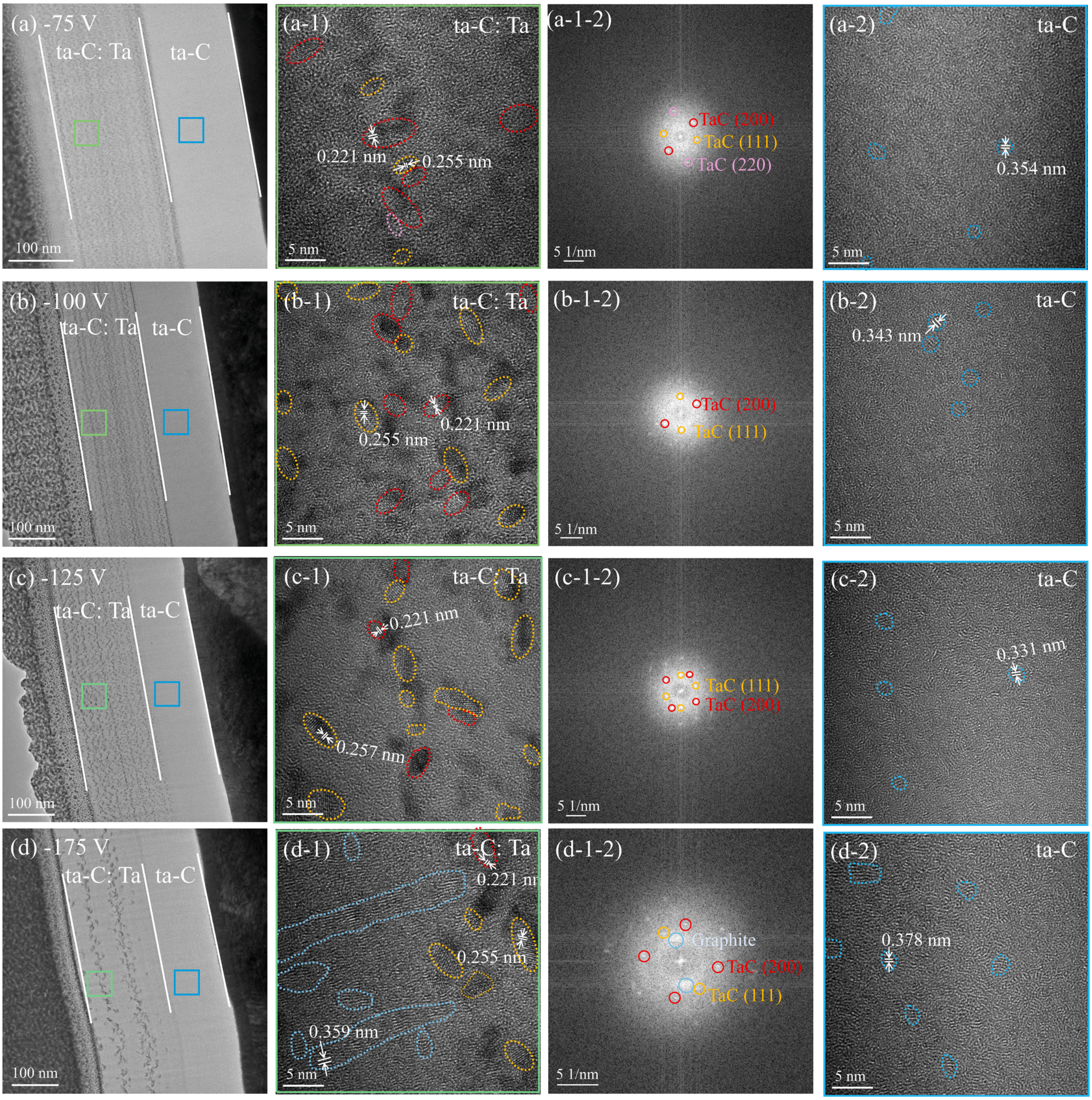

Fig. 9. Cross-sectional HRTEM images of the coatings (a) −75 V, (b) −100 V, (c) −125 V, (d) −175 V, (a-1) high-resolution (640 k magnification) TEM image of the green boxed region in Fig. 9(a), (b-1) high-resolution (640 k magnification) TEM image of the green boxed region in Fig. 9(b), (c-1) high-resolution (640 k magnification) TEM image of the green boxed region in Fig. 9(c), (d-1) high-resolution (640 k magnification) TEM image of the green boxed region in Fig. 9(d), (a-1–2) FFT (Fast Fourier Transform) image of Fig. 9(a-1), (b-1–2) FFT (Fast Fourier Transform) image of Fig. 9(b-1), (c-1–2) FFT (Fast Fourier Transform) image of Fig. 9(c-1), (d-1–2) FFT (Fast Fourier Transform) image of Fig. 9(d-1), (a-2) high-resolution (640 k magnification) TEM image of the blue boxed region in Fig. 9(a), (b-2) high-resolution (640 k magnification) TEM image of the blue boxed region in Fig. 9(b), (c-2) high-resolution (640 k magnification) TEM image of the blue boxed region in Fig. 9(c), (d-2) high-resolution (640 k magnification) TEM image of the blue boxed region in Fig. 9(d).

[48,49]. A denser amorphous carbon structure can also effectively inhibit the penetration of corrosive species. Therefore, the formation of the TaC (111) structure and denser amorphous carbon structure in the coating deposited at −125 V bias voltage results in fewer chemically active sites and lower corrosion defect density compared to the coating deposited at −75 V bias voltage. Compared with the amorphous carbon structure, the formation of graphite structure in the coating deposited at −175 V bias voltage displays lower interlayer attractive energy, larger interlayer spacing and stronger electrical conductivity, which provides a penetration path for the corrosive species, enhances the charge transfer process, and demonstrates lower chemical stability [50,51]. Therefore, the formation of graphite structure in ta-C: Ta layer and higher graphite nanocrystal spacing in the ta-C layer contributes to the highest corrosive defect depth of the coating deposited at −175 V bias voltage.

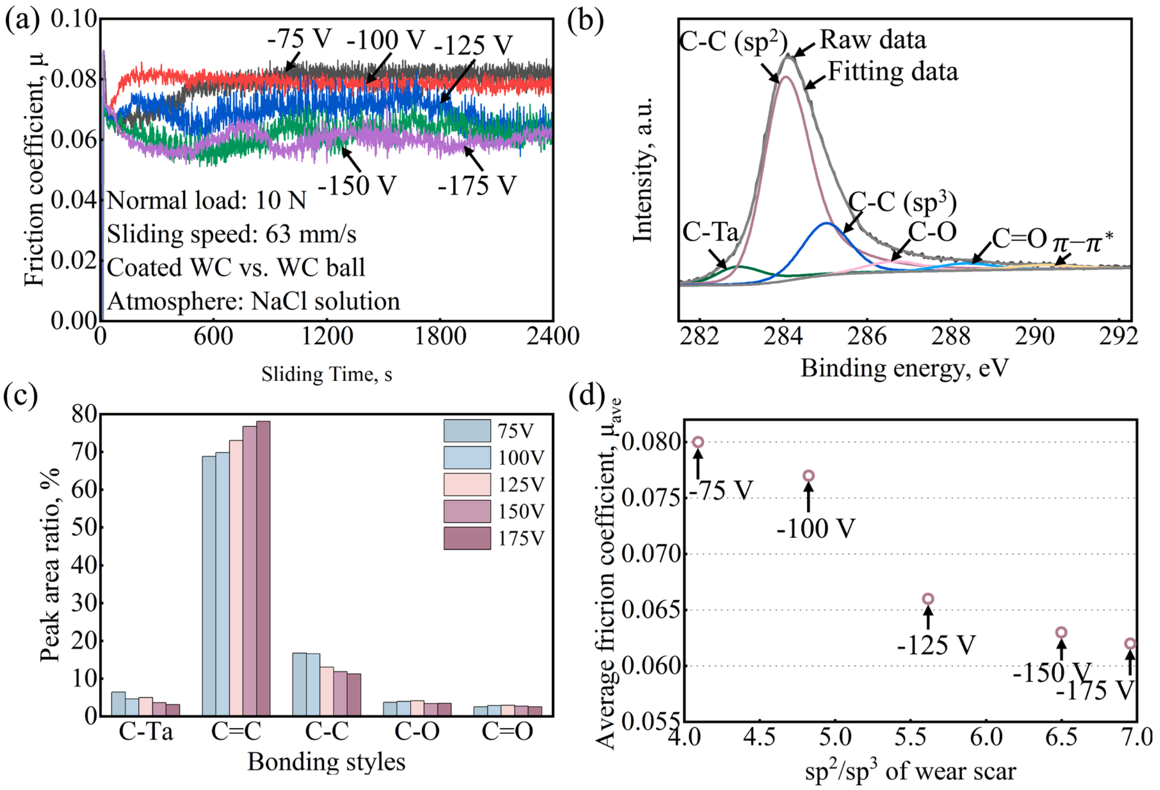

Fig. 10. Friction behavior of coatings (a) friction coefficient of the coatings, (b) representative C1s deconvolution result (-75 V) in the wear scar, (c) deconvoluted peak area ratios of coatings at bias voltage decreasing from −75 V to −175 V, (d) relationship between friction coefficient and the sp^2/sp^3 ratio in the wear scar.

3.3. *Tribological properties of the coatings*

3.3.1. *Friction behavior of the coatings*

Quantified friction coefficient measurements during immersed sliding contact in sodium chloride solution exhibited variations corresponding to deposition bias voltage. As the deposition bias voltage decreases from −75 V to −125 V, Fig. 10 (a) shows that the friction coefficients were 0.08 and 0.077 for deposition bias voltages at −75 V and −100 V, respectively. For the coating deposited at −125 V bias voltage, the friction coefficient decreased slightly after 1800 s, reaching 0.066 by the end of the test. As the deposition bias voltage decreased to −150 V and −175 V, the coatings exhibited slight fluctuations throughout the sliding process, and the friction coefficients decreased significantly, ultimately reaching final values of 0.063 and 0.062, respectively. The varying friction coefficients indicate that the deposition bias voltage affects the tribological properties of the coatings.

Generally, surface characteristics, particularly reduced surface roughness and elevated sp^2/sp^3 ratio, are key factors that reduce interfacial shear resistance during the sliding process [52,53]. However, experimental analysis revealed that all coatings in this study exhibit comparable surface roughness values. This suggests that the variations observed in the friction coefficient must be attributed to factors beyond surface roughness. Analyzing how the carbon structure influences the friction coefficient proves crucial. XPS analysis was conducted to characterize the sp^2/sp^3 ratio in the wear scar on the coatings. The C1s deconvolution result, presented in Fig. 10 (b), revealed multiple bond structures like those observed in the as-deposited coatings (shown in Fig. 3(a)). The chemical bonds include C-Ta, C-C sp^2, C-C sp^3, C-O, C═O, and π electron shake-up. Fig. 10 (d) shows the relationship between the friction coefficient and the sp^2/sp^3 ratio (derived from the deconvoluted peak area ratio results presented in Fig. 10 (c)). The sp^2/sp^3 ratio correlates negatively with measured friction coefficients. This finding suggests that bias voltage modulation provides a direct method for self-lubricating surfaces through controlled graphitic transformation processes during deposition. The lowest friction coefficient was correlated with the maximum sp^2/sp^3 ratio value achieved in the coating deposited at −175 V bias voltage.

Regarding the stable and fluctuating sliding processes of the coating deposited at bias voltages of −100 V and −175 V, Fig. 11 displays the wear surface characteristics of the WC sphere through laser imagery and Raman spectra data. As shown in Fig. 11 (a, b), the WC sphere surface that contacted with coatings displays the blank region (indicated as point 1), black damage region, and yellow region (indicated as point 2, only for coating deposited at a bias voltage of −100 V). The black damage regions remained isolated from direct contact with the coating throughout the friction coefficient evaluation period. The characteristics of the friction-affected region (indicated as points 1 and 2) are critical for understanding the sliding process. Fig. 11 (c) shows the Raman spectral analysis conducted on the friction-affected regions (indicated as point 1 and point 2). While the tungsten carbide, tungsten oxide, and tantalum oxide are present at point 1 for all coatings, point 2 for the coating deposited at a bias voltage of −100 V exhibits an obvious graphitized peak. Profilometric analysis of the WC wear surface, shown in Fig. 11 (d), reveals distinctive material accumulation where it contacted with the coating deposited at −100 V bias voltage. The formation of an accumulated graphitized transfer layer is the main factor contributing to the stable sliding process observed for the coating deposited at a bias voltage of −100 V. Based on the HRTEM observations in Fig. 9, the fluctuating sliding process observed at −175 V bias voltage can be attributed to competing mechanisms: the formation of lubricating graphite structures and the resulting decrease in mechanical strength. The decreased mechanical strength appears to cause coating damage during the sliding process and results in friction coefficient fluctuations.

3.3.2. *Wear properties of the coatings*

Fig. 12 shows the wear scar images of coatings tested in sodium chloride solution. As shown in Fig. 12 (a-e), with decreasing deposition bias voltage from −75 V to −175 V, only the coatings deposited at bias

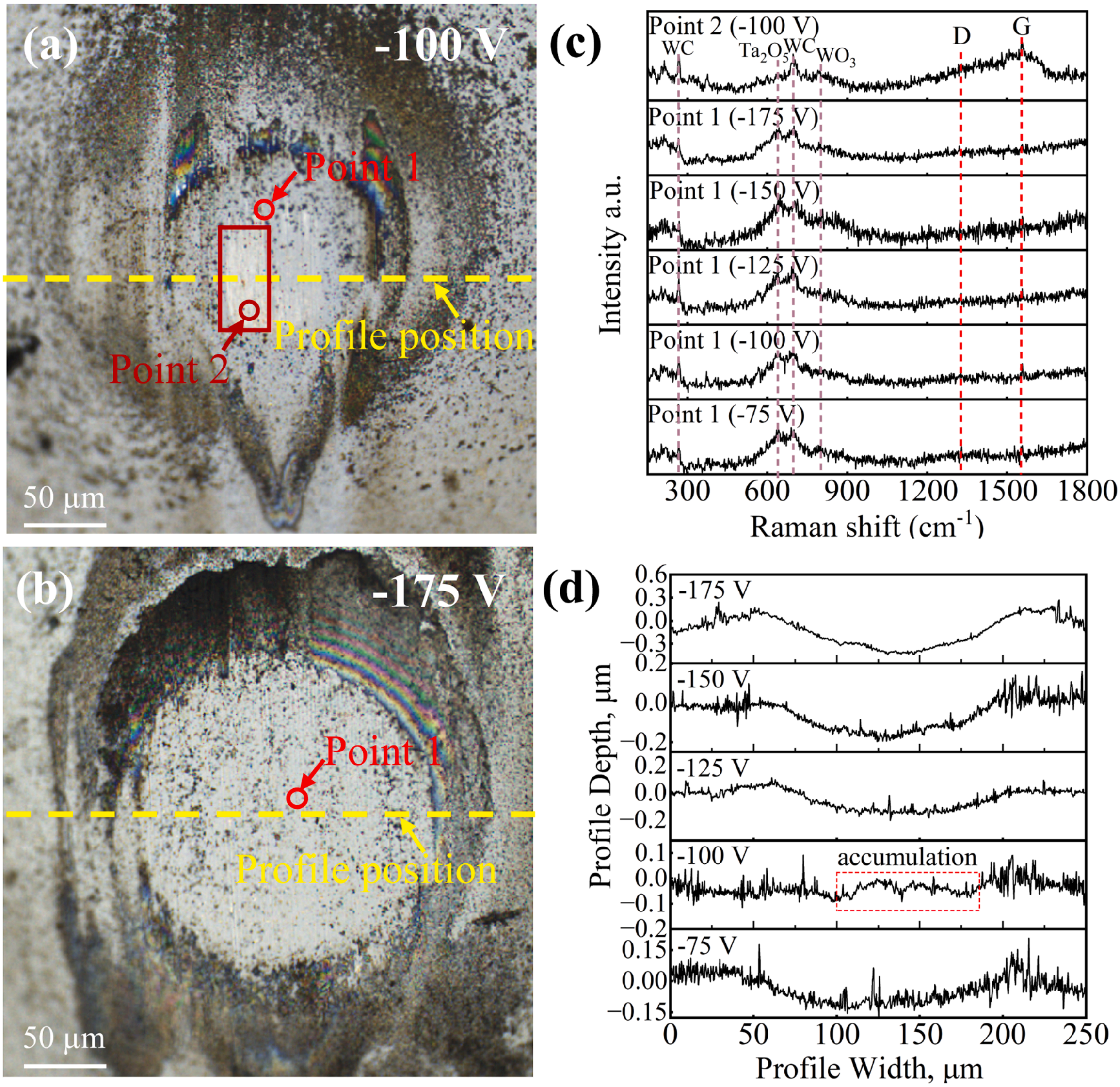

Fig. 11. Wear surface properties of the WC counterpart sphere (a) Laser images of the wear surface on the WC sphere after testing against the coating at bias voltage of −100 V, (b) Laser images of the wear surface on the WC sphere after testing against the coating at bias voltage of −175 V, (c) Raman spectra analysis conducted on the friction-affected region, (d) Wear profile of the worn WC sphere after testing against the coatings.

voltages of −100 V and −125 V display normal wear. In addition to normal wear, peeling off is observed on coatings deposited at bias voltages of −75 V, −150 V, and −175 V (highest peeling off density). Fig. 13 (a) shows the specific wear rate of the coatings. As the deposition bias voltage decreases from −75 V to −100 V and −125 V, the wear rate decreases from 3.36 to 2.78 and 2.94 × 10^{-8} mm^3/Nm, respectively. The wear rate escalates significantly to 4.96 × 10^{-8} mm^3/Nm as the deposition bias voltage decreases to −175 V. The various wear patterns and specific wear rates suggest that deposition bias voltage functions as a key determinant in the wear properties of the coatings.

The absence of chemical degradation in the wear scar directs analytical focus toward mechanical properties, particularly the contribution of hardness to wear resistance mechanisms [54]. Fig. 13 (b, c) shows the nanoindentation curves and the calculated hardness. Unlike the other coatings that only display normal indentation processes, the coating deposited at a bias voltage of −175 V exhibits several parallel indentation points (indicated as a red dashed circle). As shown in Fig. 13 (d), the analysis of the correlation between hardness and wear rate reveals a negative correlation, indicating that higher hardness corresponds to improved wear resistance. Coatings deposited at bias voltages of −100 V and −125 V exhibit higher hardness than other coatings, resulting in lower wear rates, while the coating deposited at −175 V bias voltage exhibits the lowest hardness and consequently the highest wear rate. Generally, the coating bonding structure is a key factor affecting its hardness [55,56]. However, it is worth noting that neither the I_D/I_G ratio obtained from Raman spectra nor the sp^2/sp^3 ratio obtained from XPS analysis (through coating thickness) directly correlates with the hardness values. The results suggest that the distribution of tantalum bonding structures continues to play a critical role in determining hardness. Analysis of the HRTEM images in Fig. 9 reveals that as the deposition bias voltage decreases from −75 V to −125 V, the preferential orientation of the tantalum carbide structure shifts from TaC (200) to TaC (111). Compared to the TaC (200), the preferential growth of TaC (111) nanocrystals in the coating provides enhanced resistance to plastic deformation due to its maximized coordination numbers with stronger bonding strength. This corresponds to a higher hardness observed in the coating deposited at a bias voltage of −125 V [41]. Comparing the coatings deposited at bias voltages of −100 V and −125 V, the polycrystalline structure and increased crystal density in the coating deposited at bias voltages of −100 V led to enhanced deformation resistance and the highest hardness [56,57]. In contrast, the graphite structure formed in the coating deposited at −175 V, with its lower

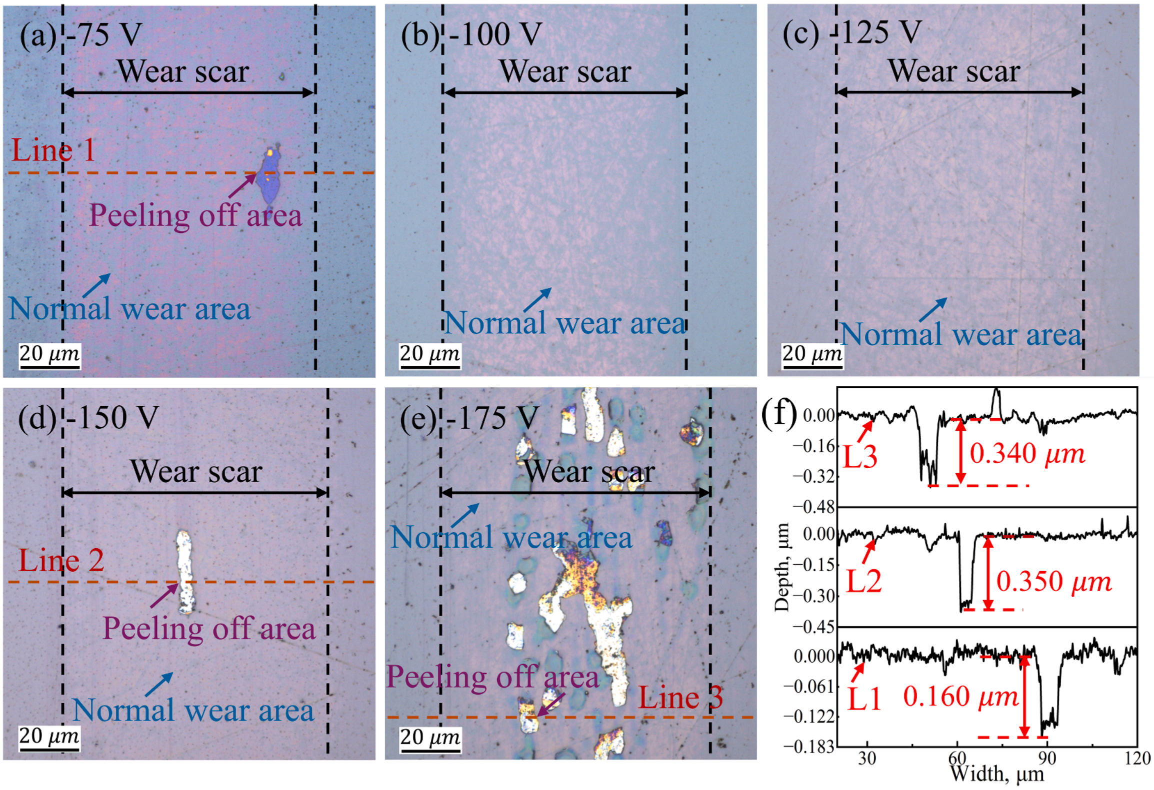

Fig. 12. Wear scar images of the coatings at various bias voltages when tested in sodium chloride solution (a) −75 V, (b) −100 V, (c) −125 V, (d) −150 V, (e) −175 V, and (f) profile of the peeling off area in the wear scar.

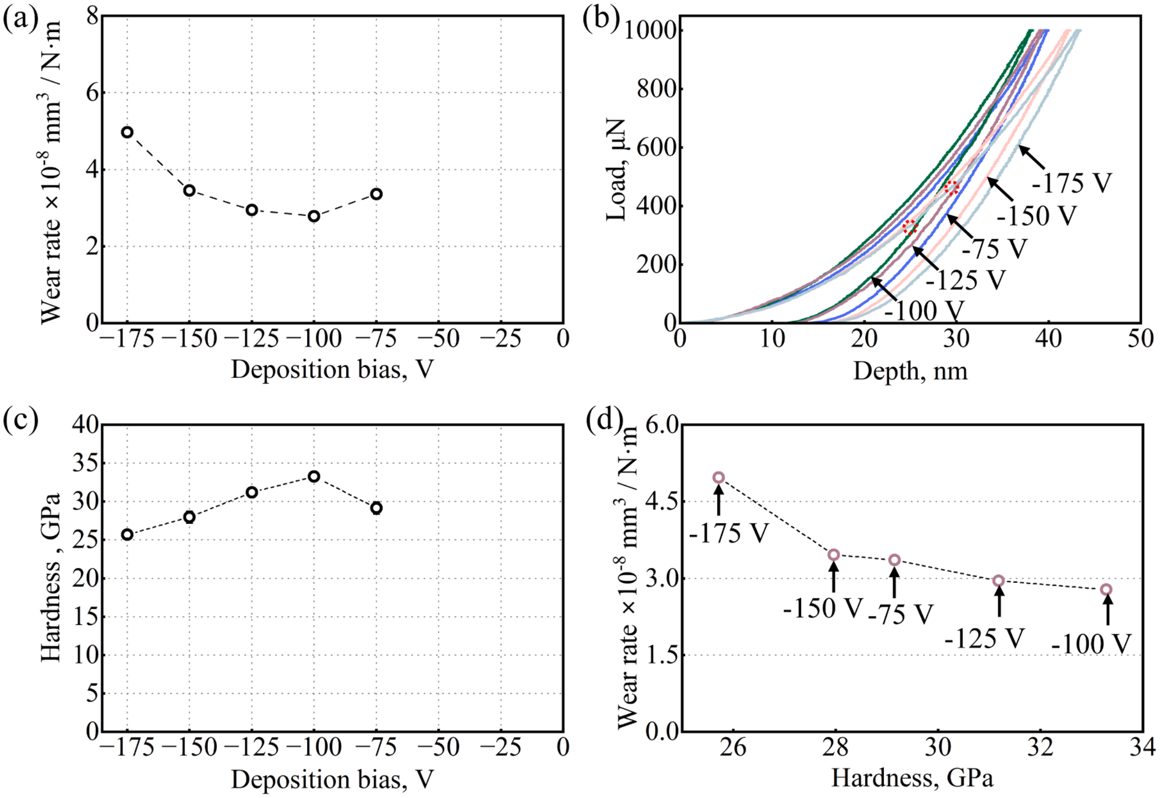

Fig. 13. Wear properties of coatings when tested in sodium chloride solution (a) specific wear rate of the coatings at bias voltage decreasing from −75 V to −175 V, (b) nanoindentation curves of the coatings at bias voltage decreasing from −75 V to −175 V, (c) hardness values of the coatings at bias voltage decreasing from −75 V to −175 V, (d) relationship between specific wear rate and hardness of the coatings at bias voltage decreasing from −75 V to −175 V.

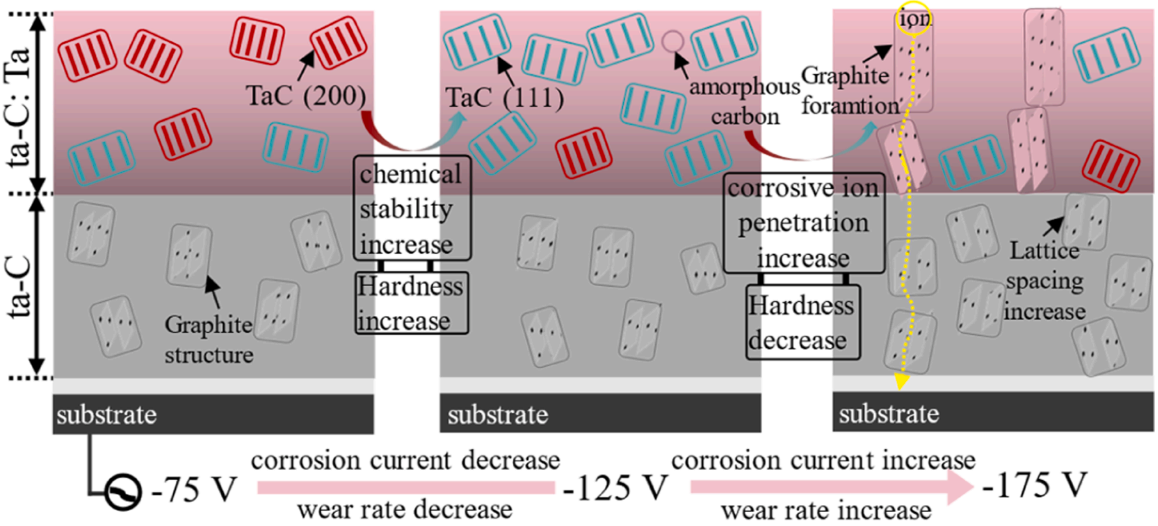

Fig. 14. The schematic of corrosion and wear mechanisms of coatings when tested in sodium chloride solution.

interlayer attractive energy and larger interlayer spacing, decreased deformation resistance and hardness.

Fig. 14 presents a framework that illustrates the mechanisms influencing electrochemical behavior and wear properties. This comprehensive visualization depicts the correlation between deposition bias voltage and the resulting structural properties, which determine corrosion current density and wear response. Specifically, the bias voltage of −125 V promotes preferential growth of TaC (111) nanocrystalline structure with a superior chemical stability and mechanical strength, resulting in enhanced resistance to chemical corrosion and wear removal. Conversely, the bias voltage of −175 V induces extensive carbon network reorganization toward the graphite structure, which creates pathways for corrosive species transport and compromises the mechanical load-bearing capacity of the coating.

4. Conclusions

In this study, we prepared bilayer coatings (ta-C bottom layer followed by a Ta-containing top layer), focusing on how the applied deposition bias voltage optimizes corrosion resistance and tribological properties. This investigation demonstrates that deposition bias voltage serves as a critical parameter that adjusts the bond structure of the coatings, with an optimal value of −125 V enabling the preferential growth of TaC (111) nanocrystal domains embedded in a dense amorphous carbon matrix. The preferential growth of TaC (111) nanocrystals, with its stronger bonding strength and higher surface cleavage energy, shows a superior chemical stability and mechanical strength, resulting in excellent corrosion current ($\log i = -7.93$) and wear rate (2.94×10^{-8} mm^3/Nm). Comparing the structure of the coating deposited at a bias voltage of −125 V, the formation of a polycrystalline structure and increased crystal density in the coating deposited at a bias voltage of −100 V led to enhanced deformation resistance, corresponding to the highest hardness and the lowest wear rate (2.78×10^{-8} mm^3/Nm). Bias voltage of −175 V induces carbon network reorganization toward the graphite structure, resulting in the lowest friction coefficient (0.062). However, the decreased mechanical strength led to the fluctuating sliding processes, coating peeling damage, and the highest wear rate (4.96×10^{-8} mm^3/Nm).

CRediT authorship contribution statement

Ruixi Zhang: Writing – review & editing, Validation. **Wenjun Wu:** Writing – review & editing, Validation. **Xue Fan:** Writing – review & editing, Validation. **Nan Jian:** Writing – review & editing, Data curation. **Dongfeng Diao:** Writing – review & editing. **Noritsugu Umehara:** Writing – review & editing, Supervision. **Li LuLu:** Writing – original draft, Visualization, Validation, Investigation, Formal analysis, Data curation, Conceptualization. **Takayuki Tokoroyama:** Writing – review & editing, Supervision, Project administration, Methodology, Funding acquisition, Formal analysis.

Declaration of Competing Interest

The authors declare no conflicts of interest associated with this manuscript.

Acknowledgments

Part of this research was conducted with the support of Human Resource Development and Research Project on Production Technology for the Aerospace Industry: Subsidy from Gifu Prefecture, MEXT KAKENHI Grant Number JP23H01327, JST FOREST Program, Grant Number: JPMJFR212E.

Data availability

Data will be made available on request.

References

[1] dos Santos C, de Almeida N, Panossian Z, Tiroel L, Jorge V, Oliveira E. Stress corrosion cracking in fuel-grade anhydrous ethanol from dedicated and multi-products pipelines. Eng Fail Anal 2021;125:105426. https://doi.org/10.1016/j.engfailanal.2021.105426.
[2] Masripan N, Ohara K, Umehara N, Kousaka H, Tokoroyama T, Inami S, Zushi K, Fujita M. Hardness effect of DLC on tribological properties for sliding bearing under boundary lubrication condition in additive-free mineral base oil. Tribol Int 2013;65:265–9. https://doi.org/10.1016/j.triboint.2013.01.016.
[3] Taib M, Umehara N, Tokoroyama T, Murashima M. The effects of oil additives and mating materials to the friction, wear and seizure characteristics of a-C:H coating. J Tribol 2018;18:1–9. ⟨https://jurnaltribologi.mytribos.org/v18/JT-18-1-19.pdf⟩.
[4] Aboua K, Umehara N, Kousaka H, Tokoroyama T, Murashima M, Mabuchi Y, Higuchi T, Kawaguchi M. Effect of carbon diffusion on friction and wear behaviors of diamond-like carbon coating against Cr-plating in boundary base oil lubrication. Tribol Online 2018;13:290–300. https://doi.org/10.2474/trol.13.290.
[5] Aboua K, Umehara N, Kousaka H, Tokoroyama T, Murashima M, Mabuchi M, Higuchi T, Kawaguchi M. Effect of carbon diffusion on friction and wear behaviors of diamond-like carbon coating against germanium in boundary base oil lubrication. Tribol Lett 2019;67:65. https://doi.org/10.1007/s11249-019-1179-2.
[6] Zhang R, Lee W, Umehara N, Tokoroyama T, Murashima M, Takimoto Y. The development of B/Cr co-doped DLC coating by FCVA deposition system and its tribological properties at 300 °C. Surf Coat Technol 2024;487:130968. https://doi.org/10.1016/j.surfcoat.2024.130968.

[7] Tokoroyama T, Murashima M, Umehara N. The surface enhanced raman scattering analysis for carbonaceous coating by using Au nano-particles. Tribol Online 2020; 15:300–8. https://doi.org/10.2474/trol.15.300.

[8] Tokoroyama T, Goto M, Umehara N, Nakamura T, Honda F. Effect of Nitrogen atoms desorption on the friction of the CNx coating against Si_3N_4 ball in Nitrogen gas. Tribol Lett 2006;22:215–20. https://doi.org/10.1007/s11249–006–9084–x.

[9] Tokoroyama T, Kamiya M, Umehara N, Wang C, Diao D. Influence of UV irradiation in low frictional performance of CN $_x$ coatings. Lubr Sci 2012;24: 129–39. https://doi.org/10.1002/ls.1168.

[10] Tokoroyama T, Hattori T, Umehara N, Kousaka H, Manabe K, Kishi M, Fuwa Y. Ultra-low friction properties of carbon nitride tantalum coatings in the atmosphere. Tribol Int 2016;103:388–93. https://doi.org/10.1016/j.triboint.2016.07.015.

[11] Nagai T, Hiratsuka M, Alanazi A, Nakamori H, Hirakuri K. Anticorrosion of DLC coating in acid solutions. Appl Surf Sci 2021;552:149373. https://doi.org/10.1016/j.apsusc.2021.149373.

[12] Dalibón E, Escalada L, Simison S, Forsich C, Heim D, Brühl S. Mechanical and corrosion behavior of thick and soft DLC coatings. Surf Coat Technol 2017;312: 101–9. https://doi.org/10.1016/j.surfcoat.2016.10.006.

[13] Wei J, Li H, Liu L, Guo P, Ke P, Wang A. Enhanced tribological and corrosion properties of multilayer ta-C films via alternating sp3 content. Surf Coat Technol 2019;374:317–26. https://doi.org/10.1016/j.surfcoat.2019.05.08.

[14] Hu K, Hu S, Zeng S, Peng B, Xiong X, Wang W, Cheng G. The effect of surface treatment on the corrosion behavior of pure Ta sheet in an equimolar NaCl-KCl melt at 850℃ in air, part 2: diamond film, TaC film, Ta-Si coating and Ta-Si-Al coating. Corros Sci 2019;154:11–27. https://doi.org/10.1016/j.corsci.2019.03.049.

[15] Tasdemir H, Wakayama M, Tokoroyama T, Kousaka H, Umehara N, Mabuchi Y, Higuchi T. Ultra-low friction of tetrahedral amorphous diamond-like carbon (ta-C DLC) under boundary lubrication in poly alpha-olefin (PAO) with additives. Tribol Int 2013;65:286–94. https://doi.org/10.1016/j.triboint.2013.03.014.

[16] Mustafa MMBin, Umehara N, Tokoroyama T, Murashima M, Shibata A, Utsumi Y, Moriguchi H. Effect of mesh structure of tetrahedral amorphous carbon (ta-C) coating on friction and wear properties under base-oil lubrication condition. Tribol Int 2020;147:105557. https://doi.org/10.1016/j.triboint.2019.01.016.

[17] Liu X, Yamaguchi R, Umehara N, Murashima M, Tokoroyama T. Effect of oil temperature and counterpart material on the wear mechanism of ta-CNx coating under base oil lubrication. Wear 2017;390–391:312–21. https://doi.org/10.1016/j.wear.2017.08.012.

[18] Liu X, Umehara N, Tokoroyama T, Murashima M. Tribological properties of ta-CNx coating sliding against steel and sapphire in unlubricated condition. Tribol Int 2019;131:102–11. https://doi.org/10.1016/j.triboint.2018.10.022.

[19] Lee W, Jang Y, Tokoroyama T, Murashima M, Umehara N. Effect of defects on wear behavior in ta-C coating prepared by filtered cathodic vacuum arc deposition. Diam Relat Mater 2020;105:107789. https://doi.org/10.1016/j.diamond.2020.107789.

[20] Hashizume N, Murashima M, Umehara N, Tokoroyama T, Lee W. In situ observation of the formation of MoDTC-derived tribofilm on a ta-C coating using reflectance spectroscopy and its effects on friction. Tribol Int 2021;162:107128. https://doi.org/10.1016/j.triboint.2021.107128.

[21] Nishimura H, Umehara N, Kousaka H, Tokoroyama T. Clarification of relationship between friction coefficient and transformed layer of CNx coating by in-situ spectroscopic analysis. Tribol Int 2016;93:660–5. https://doi.org/10.1016/j.triboint.2014.12.015.

[22] Lee W, Tokoroyama T, Jang Y, Umehara N. Effect of substrate bias and temperature on friction and wear properties for ta-C coating prepared under different substrate bias voltages with filtered cathodic vacuum arc deposition. Tribol Online 2018;13: 241–7. https://doi.org/10.2474/trol.13.241.

[23] Tokoroyama T, Tagami Y, Murashima M, Lee W, Umehara N, Kousaka H. Tribological property of ta-CNx:Ta deposited via ion beam assisted-filtered arc deposition. Tribol Int 2022;168:107450. https://doi.org/10.1016/j.triboint.2022.107450.

[24] Nyberg H, Tokoroyama T, Wiklund U, Jacobson S. Design of low-friction PVD coating systems with enhanced running-in performance — carbon overcoats on TaC/aC coatings. Surf Coat Technol 2013;222:48–54. https://doi.org/10.1016/j.surfcoat.2013.02.003.

[25] Li L, Tokoroyama T, Zhang R, Umehara N. Corrosion and tribological properties of ta-C/ta-C: Ta coatings: analysis of the influence of Ta-O/Ta-C ratio. Tribol Int 2024; 198:109916. https://doi.org/10.1016/j.triboint.2024.109916.

[26] Fayed S, Chen D, Li S, Zhou Y, Wang H, Sadawy M. Corrosion behavior and passive stability of multilayer DLC-Si coatings. Surf Coat Technol 2022;431:128001. https://doi.org/10.1016/j.surfcoat.2021.128001.

[27] Ren L, Liu X, Cao H, Tang Y, Qi F, Zhao N, Dai Y, Ouyang X. Mechanical and corrosion properties of hydrogen-free DLC coatings prepared on degradable as-extruded WE43 alloy using FCVA technology. Surf Coat Technol 2024;476:130293. https://doi.org/10.1016/j.surfcoat.2023.130293.

[28] Han C, Yang T, Lin X, Song Y, Xie M, Deng Q, Wen F. Effect of bias gradient delta on mechanical and tribological properties of DLC films sputtered on ACM. Surf Coat Technol 2024;481:130626. https://doi.org/10.1016/j.surfcoat.2024.130626.

[29] Saha D. S. Negative dc substrate bias influencing the low-temperature growth of B-doped DLCs in a low-pressure rf inductive plasma. Diam Relat Mater 2024;146: 111219. https://doi.org/10.1016/j.diamond.2024.111219.

[30] Li H, Sun P, Qi A, Zhang S, Zhang F. Modulation of structure and corrosion behavior of Si-DLC coatings on AZ31 by applying a self-source bias. Ceram Int 2023;49:32193–204. https://doi.org/10.1016/j.ceramint.2023.07.194.

[31] Wu W, Murashima M, Saso T, Tokoroyama T, Lee W, Kousaka H, Umehara N. New in situ superlow-friction method for nitrogen-containing diamond-like carbon coatings using dielectric barrier discharge treatment in ambient air. Tribol Int 2022;174:107749. https://doi.org/10.1016/j.triboint.2022.107749.

[32] McCafferty E. Validation of corrosion rates measured by the Tafel extrapolation method. Corros Sci 2005;47:3205–17. https://doi.org/10.1016/j.corsci.2005.05.046.

[33] Poorqasemi E, Abootalebi O, Peikari M, Haqdar F. Investigating accuracy of the Tafel extrapolation method in HCl solutions. Corros Sci 2009;51:1043–54. https://doi.org/10.1016/j.corsci.2009.03.001.

[34] Lu Y, Huang G, Song X, Wang H, Pan J. Influence of Si content on infrared and electrical properties of metal-free transparent conductive Si-doped dlc film. Diam Relat Mater 2024;151:111854. https://doi.org/10.1016/j.diamond.2024.111854.

[35] Lu S, Ding J, Wei X, Lee K, Chen Z, Yang W, Qiao J, Chen K, Zhang D, Zhang W, Li X. Structural modulation and frictional, antibacterial and biocompatible properties of Ag-incorporated DLC films: dependence on Ag precipitation behavior. Appl Surf Sci 2024;677:161078. https://doi.org/10.1016/j.apsusc.2024.161078.

[36] Cheng Y, Cai W, Li H, Zheng Y, Zhao L. Surface characteristics and corrosion resistance properties of TiNi shape memory alloy coated with Ta. Surf Coat Technol 2004;186:346–52. https://doi.org/10.1016/j.surfcoat.2004.01.012.

[37] Cheng Y, Cai W, Zheng Y, Li H, Zhao L. Surface characterization and immersion tests of TiNi alloy coated with Ta. Surf Coat Technol 2004;190:428–33. https://doi.org/10.1016/j.surfcoat.2004.03.051.

[38] Xiao Z, Ren L, Guo C, Liang L, Dai Y, Tang K, Lu L, Qi F, She J, Wang L, Ouyang X. Enhanced corrosion resistance, mechanical properties, and biocompatibility of N-DLC coatings prepared on WE43 alloy via FCVA technology. J Alloy Compd 2024; 1010:178106. https://doi.org/10.1016/j.jallcom.2024.178106.

[39] Wu H, Shi Z, Zhang X, Qasim A, Xiao S, Zhang F, Wu Z, Wu G, Ding K, Chu P. Achieving an acid resistant surface on magnesium alloy via bio-inspired design. Appl Surf Sci 2019;478:150–61. https://doi.org/10.1016/j.apsusc.2019.01.181.

[40] Etula J, Wester N, Liljeström T, Sainio S, Palomäki T, Arstila K, Sajavaara T, Koskinen J, Caro M, Laurila T. What determines the electrochemical properties of nitrogenated amorphous carbon thin films? Chem Mat 2021;33(17):6813–24. https://doi.org/10.1021/acs.chemmater.1c01519.

[41] Wang C, Sui X, Lu X, Zhang X, Yan Z, Lu Y, Hao J. Friction and wear of a-C:H films deposited at different bias in air and NaCl solution. Tribol Int 2022;175:107863. https://doi.org/10.1016/j.triboint.2022.107863.

[42] Daroonparvar M, Khan M, Saadeh Y, Kay C, Kasar A, Kumar P, Esteves L, Misra M, Menezes P, Kalvala P, Bakhsheshi-Rad H, Gupta R. Modification of surface hardness, wear resistance and corrosion resistance of cold spray Al coated AZ31B Mg alloy using cold spray double layered Ta/Ti coating in 3.5 wt% NaCl solution. Corros Sci 2020;176:109029. https://doi.org/10.1016/j.corsci.2020.109029.

[43] Rahimi E, Nijdam T, Jahagirdar A, Broitman E, Mol A. Improved surface charge and corrosion resistance at the near-nanocrystalline chromium/nano-bilayer oxide interface in advanced thin dense chromium coatings. Appl Surf Sci 2025;689: 162504. https://doi.org/10.1016/j.apsusc.2025.162504.

[44] Cao L, Liu J, Wan Y, Pu J. Corrosion and tribocorrosion behavior of W doped DLC coating in artificial seawater. Diam Relat Mater 2020;109:108019. https://doi.org/10.1016/j.diamond.2020.108019.

[45] Wei X, Feng H, Liu Z, Chen Z, Yin P, Lu S, Ding J, Du N, Li X, Zhang G. Insight into the corrosion behaviors and mechanism of the self-healing Si/N-DLC films in oilfield environment. Corros Sci 2024;231:111989. https://doi.org/10.1016/j.corsci.2024.111989.

[46] Kim H, Ahn S, Kim J, Park S, Lee K. Effect of Si-incorporation on wear–corrosion properties of diamond-like carbon films. Thin Solid Films 2004;482:299–304. https://doi.org/10.1016/j.tsf.2004.11.164.

[47] Wei J, Guo P, Liu L, Li H, Li H, Wang S, Ke P, Saito H, Wang A. Corrosion resistance of amorphous carbon film in 3.5 wt% NaCl solution for marine application. Electro Acta 2020;346:136282. https://doi.org/10.1016/j.electacta.2020.136282.

[48] Kwon S, Rajkamal A, An J, Yun G. Mechanisms of oxycarbide formation on ZrC, HfC, and TaC surfaces during early oxidation: Insights from computational simulations. Ceram Int 2025. https://doi.org/10.1016/j.ceramint.2025.01.317.

[49] Quesne M, Roldan A, de Leeuw N, Catlow C. Bulk and surface properties of metal carbides: implications for catalysis. Phys Chem Chem Phys 2018;20:6905–16. https://doi.org/10.1039/C7CP06336A.

[50] Nakajima T, Touma M. Surface free energy and chemical bonding of fluorine-graphite intercalation compounds. J Fluor Chem 1992;57:83–91. https://doi.org/10.1016/S0022-1139(00)82819-5.

[51] Benedict L, Chopra N, Cohen M, Zettl A, Louie S, Crespi V. Microscopic determination of the interlayer binding energy in graphite. Chem Phys Lett 1998; 286:490–6. https://doi.org/10.1016/S0009-2614(97)01466-8.

[52] Jin L, Li Y, Liu C, Fan X, Zhu M. Friction mechanism of DLC/MAO wear-resistant coatings with porous surface texture constructed in-situ by micro-arc oxidation. Surf Coat Technol 2023;473:130010. https://doi.org/10.1016/j.surfcoat.2023.130010.

[53] Wang X, Zhang X, Wang C, Lu Y, Hao J. High temperature tribology behavior of silicon and nitrogen doped hydrogenated diamond-like carbon (DLC) coatings. Tribol Int 2022;175:107845. https://doi.org/10.1016/j.triboint.2022.107845.

[54] Hassani S, Raeissi K, Azzi M, Li D, Golozar M, Szpunar J. Improving the corrosion and tribocorrosion resistance of Ni–Co nanocrystalline coatings in NaOH solution. Corros Sci 2009;51:2371–9. https://doi.org/10.1016/j.corsci.2009.06.026.

[55] He D, Shang L, Feng Z, Zhao Y, Li W, Zhai H, Cheng B, Zhang X. Role of carbide content in governing the mechanical and tribological properties of DLC/

Cr3C2–NiCr duplex coatings. Tribol Int 2023;187:108687. https://doi.org/10.1016/j.triboint.2023.108687.

[56] Javidparvar A, Mosavi M, Ramezanzadeh B. Nickel-aluminium bronze (NiBRAl) casting alloy tribological/corrosion resistance properties improvement via deposition of a Cu-doped diamond-like carbon (DLC) thin film; optimization of sputtering magnetron process conditions. Mater Chem Phys 2023;296:127279. https://doi.org/10.1016/j.matchemphys.2022.127279.

[57] Zhang S, Sun D, Fu Y, Du H. Recent advances of superhard nanocomposite coatings: a review. Surf Coat Technol 2003;167:113–9. https://doi.org/10.1016/S0257-8972(02)00903-9.